Author's Accepted Manuscript

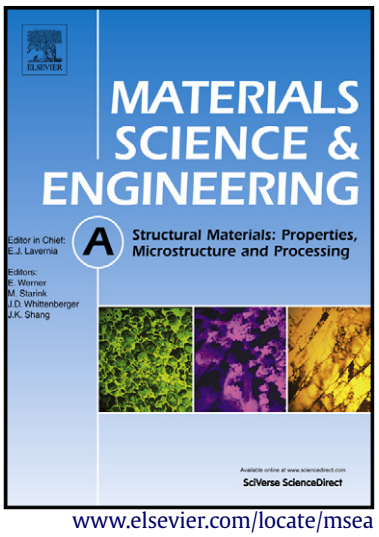

www.elsevier.com/locate/msea

Selective laser melting of an $Al_{86}Ni_6Y_{4.5}Co_2La_{1.5}$ metallic glass: processing, microstructure evolution and mechanical properties

X.P. Li, C.W. Kang, H. Huang, L.C. Zhang, T.B. Sercombe

PII: S0921-5093(14)00388-8
DOI: http://dx.doi.org/10.1016/j.msea.2014.03.097
Reference: MSA30946

To appear in: *Materials Science & Engineering A*

Received date: 27 February 2014
Revised date: 24 March 2014
Accepted date: 25 March 2014

Cite this article as: X.P. Li, C.W. Kang, H. Huang, L.C. Zhang, T.B. Sercombe, Selective laser melting of an $Al_{86}Ni_6Y_{4.5}Co_2La_{1.5}$ metallic glass: processing, microstructure evolution and mechanical properties, *Materials Science & Engineering A*, http://dx.doi.org/10.1016/j.msea.2014.03.097

Selective laser melting of an $Al_{86}Ni_6Y_{4.5}Co_2La_{1.5}$ metallic glass: processing, microstructure evolution and mechanical properties

X.P. Li [a,*], C.W. Kang [b], H. Huang [b], L.C. Zhang [c], T.B. Sercombe [a],

[a] The University of Western Australia, School of Mechanical and Chemical Engineering, Perth, WA 6009, Australia

[b] The University of Queensland, School of Mechanical and Mining Engineering, Brisbane, QLD 4072, Australia

[c] Edith Cowan University, School of Mechanical Engineering, Perth, WA 6027, Australia

[*] Corresponding author email: xiaopeng.li@uwa.edu.au

Abstract:

In this study, single line scans at different laser powers were carried out using selective laser meting (SLM) equipment on a pre-fabricated porous $Al_{86}Ni_6Y_{4.5}Co_2La_{1.5}$ metallic glass (MG) preform. The densification, microstructural evolution, phase transformation and mechanical properties of the scan tracks were systematically investigated. It was found that the morphology of the scan track was influenced by the energy distribution of the laser beam and the heat transfer competition between convection and conduction in the melt pool. Due to the Gaussian distribution of laser energy and heat transfer process, different regions of the scan track experienced different thermal history, resulting in a gradient microstructure and mechanical properties. Higher laser powers caused higher thermal stresses, which led to the formation of cracks; while low power reduced the strength of the laser track, also inducing cracking. The thermal fluctuation at high laser power produced an inhomogeneous chemical

distribution which gave rise to severe crystallization of the MG, despite the high cooling rate. The crystallization occurred both within the heat affected zone (HAZ) and at the edge of melt pool. However, by choosing an appropriate laser power crack-free scan tracks could be produced with no crystallization. This work provides the necessary fundamental understanding that will lead to the fabrication of large-size, crack-free MG with high density, controllable microstructure and mechanical properties using SLM.

Keywords: Selective laser melting; Metallic glass; Solidification microstructure; Phase transformation; Mechanical properties

1. Introduction

As a newly emerging additive manufacturing (AM) technique, selective laser melting (SLM), has undergone a rapid development for a decade [1]. It is becoming one of the most promising manufacturing techniques in the world to fabricate fully dense metal components without the need for tooling, machining or time-intensive post-processing [1]. Using a high power laser as the energy source, SLM fabricates metal components in a layer-wise manner by a complete melting and solidification mechanism. The complete melting differentiates SLM from other widely used AM techniques, e.g. direct metal laser sintering (DMLS) [1]. In SLM, the geometry of each layer is defined based on a computer aided design (CAD) model. Then the laser is scanned across the powder bed to selectively melt powder particles, which is followed by rapid solidification. After one layer is built, the build platform descends by the layer thickness (typically 50 - 100 μm) and a new layer of powder is deposited on top. During scanning of the each layer, the previously processed layer experiences surface remelting, resulting in the consolidation of adjacent powder layers. This process repeats until the entire metal component is finished. SLM has been used to fabricate a wide range of metal components including some non-ferrous metals such as Al, Ti and Ni alloys, which have potential applications in biomedical implants, automobile and aircraft industries [2-5].

Unlike conventional subtractive manufacturing techniques, SLM possesses many advantages such as fabrication of metal components with complex geometries free of expensive moulds, high materials usage efficiency together with near-net-shape formation and recycling of unmelted powder [1]. In addition, customer-designed one-off fabrication process and the production of components with different geometries in one batch are possible. Due to the high energy and the small spot size of the laser beam, only a tiny volume of material

undergoes the heating, melting and subsequent rapid solidification. This induces an extremely high temperature gradient within the material, strong thermal fluctuation in the melt pool and local shrinkage. These cause considerable accumulation of thermal stresses within the components which can give rise to micro- and macro- cracks, curling or even delamination [6, 7].

The first Al-based metallic glass (MG) was discovered in late 1980s and has attracted increasing attention due to its high specific strength and low cost in comparison to other MG materials [8]. However, due to its low glass forming ability (GFA) and thermal stability, it has taken more than two decades to fabricate the first 1 mm diameter Al-based MG ($Al_{86}Ni_6Y_{4.5}Co_2La_{1.5}$, in at. %) by copper mould casting [9]. This size limitation has constrained further investigation and improvement of the mechanical properties, especially the room temperature plasticity, greatly hindering the practical application of Al-based MG materials. Although in recent years there have been several reports of the fabrication of Al-based MG materials with diameter larger than 1 mm through hot compressing and spark plasma sintering (SPS) [10, 11], their shape and size are constrained by the die and only some simple components have been produced. More importantly, the tailoring or controlling of microstructure during such processes is extremely difficult [12, 13].

Following the concept of rapid heating and cooling a small volume of materials each time, SLM can potentially provide an alternative manufacturing method for producing large size and complex geometries from MG powder. This “point-by-point” manner may also enable the microstructure to be tailored, resulting in the formation of gradient microstructure. This heterogeneous microstructure has been reported to improve the plasticity in some MG materials [14-17]. However, SLM is a complex technique which involves complicated physical and chemical processes during fabrication. Some preliminary results have been reported on fabrication of Fe-based MG scaffolds using SLM, but there were problems with

low-density and cracking [18]. The stability, temperature gradient and thermal fluctuation in and near the melt pool have a great influence on the microstructure of final components [1]. The microstructure and properties of final components can be influenced by many other factors. Some factors are SLM-related such as laser power, laser spot size, scanning speed, scanning strategy and layer thickness. Others are materials-related such as reflectivity, heat conductivity and specific heat capacity [1]. When considering Al-based MG, their brittleness, low GFA and thermal stability, make the fabrication process even more complicated. The phase transformation (or retention of the amorphous phase) within Al-based MG during SLM can be influenced by the cooling rate and heat affected zone (HAZ). The brittleness and possible devitrification of Al-based MG will increase the risk of cracking, which is detrimental to the densification and mechanical properties of final components. However, it appears that nothing has been published regarding the processing, microstructure evolution and mechanical properties of Al-based MG materials processed using SLM.

In this work, we have systematically studied the densification, microstructure evolution and mechanical properties of an Al-based MG material processed using single line scans at different laser powers. The structure of the melt pool and HAZ and their relation to phase transformation have been assessed. The underlying mechanisms for the microstructural evolution, including crack formation and mechanical properties variation, have been explained. The aim of this work is to first demonstrate the feasibility of fabrication of marginal Al-based MG using SLM and then to establish the relationship between laser power and microstructure and mechanical properties of Al-based MG. These would further provide necessary fundamental basis for the fabrication of other MG materials using SLM.

2. Experimental procedures

2.1 Powder material

An Al-based MG powder with a spherical morphology and a composition of $Al_{86}Ni_6Y_{4.5}Co_2La_{1.5}$ (in at. %) was used for this investigation. Master ingot with a nominal composition of $Al_{86}Ni_6Y_{4.5}Co_2La_{1.5}$ (in at. %) was first prepared by arc melting high-purity elemental pieces Al (>99.9 wt. %), Ni (>99.9 wt. %), Y (>99.0 wt. %), Co (>99.9 wt. %) and La (>99.0 wt. %) under a Ti-gettered argon atmosphere for six times to ensure chemical homogeneity. Then the powder was fabricated from this master ingot through gas atomisation in high-purity nitrogen at the Institute of Metal Research, Chinese Academy of Sciences, Shenyang. Powder particles were sieved and X-ray diffraction (XRD, D/max III, Cu Kα target, operated at 40 kV and 60 mA with a step size of 0.02 ° and scanning speed 2 °/min) was used to analyse the phase formation of the sieved powder with different diameters. To ensure fully amorphous nature, only powder particles with a diameter below 25 μm were used [19].

2.2 SLM process

SLM experiments were conducted using a ReaLizer SLM-100 machine (ReaLizer GmbH, Germany) which is equipped with a fibre laser, generating a laser beam with a wavelength of 1060 nm and maximum power of 200 W at the part bed. The intensity of the laser beam can be considered to have a Gaussian distribution and the laser beam scanning can be assumed to be continuous [20].

An Al substrate (125 mm × 125 mm) is fixed on the working platform and kept at room temperature. The chamber was purged with high-purity argon gas to reduce the oxygen content to ≤ 1000 ppm.

The laser beam energy density U is critical to the fabrication process and properties of the components and for a single scan track, it is defined by [21]:

$$U = \frac{\pi P}{4vdW} \quad (1)$$

Where P is the laser power, v is the laser scan speed, d is the spot size of the laser beam and W is the thickness of the powder layer. To avoid the interference between multiple laser scan tracks and to investigate the interaction between laser beam at different laser powers and the $Al_{86}Ni_6Y_{4.5}Co_2La_{1.5}$ MG powder particles, only a single line scan was performed at each condition. According to several preliminary trials, the scanning velocity was fixed at 1000 mm/s, while the laser powers were set to be 80, 120, 160 and 200 W.

If a single line scan was conducted on loose $Al_{86}Ni_6Y_{4.5}Co_2La_{1.5}$ MG powder spread on the substrate, it was not possible to remove the samples off the substrate without damage. Therefore, the powder was lightly consolidated into a bulk form with very low density (≤ 75 % measured by the Archimedes method and close to the tap density) using SPS (SPS-1030 model, SPS SYNTEX INC, Japan) and a tungsten carbide (WC) die (outer diameter 30 mm, inner diameter 10 mm and height 20 mm). To ensure low density and avoid devitrification during SPS, a low pressure of 200 MPa and a sintering temperature of 238 °C (which is 30 °C below the powder's glass transition temperature [19]) were used without any isothermal holding. The very low density of the preform meant that it was analogous to the loose powder normally used in SLM.

2.3 Microstructure characterisation and mechanical properties

Microstructure evolution, melt pool and HAZ of the $Al_{86}Ni_6Y_{4.5}Co_2La_{1.5}$ MG processed by SLM were characterised using scanning electron microscopy (SEM, Zeiss 1555 VP-FESEM, operated at an accelerating voltage of 15 kV and working distance 10 mm). The SEM

samples were prepared in the X-Y (horizontal) and Z (vertical) cross-section (see Fig. 1). The samples were polished following the standard polishing procedures and carbon coated before SEM observation.

Nanoindentation (Hysitron® Triboindenter) was used to measure the hardness and elastic modulus of the SLM processed $Al_{86}Ni_6Y_{4.5}Co_2La_{1.5}$ MG samples at room temperature in air with a Berkovich indenter of a tip radius of 100 nm. Samples were polished but uncoated. The measurements were conducted on both the X-Y and Z cross-sections along different directions within the melt pool. The nanoindentation tests were made under the load control mode. The maximum indentation force applied was 2 mN at a rate of 200 μN/s for both loading and unloading. The dwell time was fixed at 10 s. Elastic modulus of the samples was calculated using the Oliver-Pharr method [22]. A minimum of 7 indentations were conducted on each site.

3. Results

3.1 Microstructure and phase transformation

As a layer-wise fabrication technique, SLM fabricated components are expected to show different microstructures between the horizontal (X-Y cross-section, perpendicular to the building direction) and vertical (Z cross-section, parallel to the building direction) planes (see Fig. 1). To study the microstructure and phase transformation of the SLM processed $Al_{86}Ni_6Y_{4.5}Co_2La_{1.5}$ MG, SEM back scattered images (BSE) of the scan tracks within X-Y cross-section and Z cross-section were taken and are shown in Figs. 2 and 3, respectively.

It can be seen in Fig. 2 that the width and morphology of the scan tracks (X-Y cross-section) vary with the laser power. On increasing laser power from 80 W to 200 W, the width of the

scan track increases from ~ 65 to ~ 200 μm due to the melting of more MG powder particles, which is a consequence of the higher laser energy density according to Eq. 1. The scan tracks also show different morphologies at the different laser powers. As the laser power is decreased from 200 W (Fig. 2a) to 120 W (Fig. 2c), the edge of the scan track becomes smoother. However, further decreasing the power to 80 W (Fig. 2d) increases the roughness again. When a power of 200 W is used, severe cracks are present which are vertical, parallel and at 45° to the scanning direction (white arrows in Fig. 2a). Also, pores with large diameter (~ 5 μm) form near the edge of the scan track and cracks (red arrows, in Fig. 2a). Cracks still form at a power of 160 W, but these are now only vertical and parallel to the scanning direction (Fig. 2b). Small pores (≤ 1 μm) can also be seen in the vicinity of the track edge and cracks. In contrast, no cracks and only few small pores (≤ 1 μm) can be seen at 120 W (Fig. 2c), which is indicative of better densification and microstructure. On further decreasing the laser power to 80 W (Fig. 2d), some cracks vertical and parallel to the scanning direction form again, along with an increase in the amount of porosity. The formation of the cracks and pores at relatively high laser powers (Figs. 2a and b) may be attributed to the thermal fluctuation within the melt pool during laser scan and accumulated thermal stress after rapid melting and solidification of the melt pool. While at low laser power (Fig. 2d), along with the thermal stress mentioned above, the low strength of the solidified MG caused by insufficient densification, unmelted MG powder particles and porosity may account for the formation of the cracks and pores.

In Fig. 3, it can be seen that the shape and area of the Z cross-section of the scan tracks vary with the laser power. The area of the melt pool decreases with the laser power as a result of the progressive decrease in the amount of MG particles that melt. The scan tracks exhibit a similar shape to a Gaussian distribution, indicating the anisotropy of heat flow within each single scan. At the higher laser powers, the depth of the melt pool is larger than the width

(Figs. 3a to c). However, at 80 W (Fig. 3d), the cross-section of the melt pool is sub-circular where the width of the melt pool is slightly larger than the depth, suggesting isotropy of heat flow within the melt pool. No obvious cracks can be seen in any of the vertical cross-sections of the scan tracks and only some pores can be observed. This suggests that the strength of the laser track is sufficient to withstand the accumulated thermal stress in the Z cross-section. Similar to what was found in the X-Y cross-section, the number of the pores in the Z cross-section decreases with laser power.

Unlike SLM of crystalline materials, the relaxation and devitrification behaviour of MG materials during SLM need to be considered. The phase transformation at both the center and edge of the scan tracks as well as in the HAZ has been investigated and is shown in Figs. 4 to 6, respectively. At the highest laser power, severe crystallization occurs in the center of the scan track (Fig. 4a), resulting in high Al content and low Al content crystalline areas embedded in the amorphous matrix. On lowering the laser power to 160 W (Fig. 4b), crystallization is almost completely suppressed. Only a small amount of low Al crystals (~ 2 μm in size) have precipitated from the amorphous matrix, and are concentrated in an arc-like area. Further decreasing the laser power to 120 W and 80 W (Figs. 4c and d), causes no obvious crystallization, and a featureless and homogenous microstructure. At the edge of the scan tracks, it is apparent that crystallization occurs at all laser powers (Fig. 5). Elongated crystals have formed in this region, which seem to have a preferential orientation. The higher the laser power, the larger the crystals and the more obvious the preferred orientation is. At the lowest power (Fig. 4d), the crystals appear to be more randomly oriented. Apart from the elongated crystals, equiaxed crystals with smaller size (~ 1 μm) can be observed outside the elongated crystals with a clear boundary in between.

The phase formation in the heat affected zone (HAZ) is shown in Fig. 6 with respect to the distance (L) from the edge of the melt pool. Due to the observed similarity among the HAZ

at different laser powers, only the zone at a laser power 120 W is shown here. With increasing the distance from the melt pool, the extent of crystallization decreases. Four distinct regions can be readily seen: fully crystallized region with very tiny crystals (~ 100 nm) (Fig. 6a), partially crystallized region with some bigger crystals (~ 500 nm) (Fig. 6b) and the boundary between the amorphous region and the bigger crystals region (Fig. 6c), which can be considered the edge of HAZ as no crystals can be detected in area shown in Fig. 6d.

3.2 Hardness, elastic modulus and plastic deformation behavior

The hardness and elastic modulus of the $Al_{86}Ni_6Y_{4.5}Co_2La_{1.5}$ MG processed using different laser powers were assessed using nanoindentation in the X-Y and Z cross-sections and the results are shown in Figs. 7 and 8.

Figs. 7a to c show the variation of hardness in the Z cross-section with respect to different laser powers and along three different directions, namely horizontal, vertical and 45° directions. Along the same direction, the hardness varies with the laser power. At the same laser power, the variation of the hardness differs along different directions. In Fig. 7a along the horizontal direction, the hardness decreases first from the center of the scan track outwards followed by an abrupt increase at the edge of the scan track, where the hardness exceeds that at the center. At the center of the melt pool (position 1 in Fig. 7a), the hardness shows maximum value (~ 4.7 GPa) at the highest laser power 200 W and minimum value (~ 3.8 GPa) at the lowest laser power 80 W. The hardness at a laser power of 120 W is higher than the hardness at 160 W. Mid-way between the center and edge (position 2 in Fig. 7a), the hardness is similar (~ 3.6 GPa) for all laser powers. Along the vertical direction as shown in Fig. 7b, there is a general trend of decreasing hardness from the top to the bottom of the scan track. When it comes to the 45° direction (Fig. 7c), the hardness of the MG processed with laser powers of 120 W and 160 W increases from the center to the edge, while at 80 W and

200 W the opposite occurs, with the hardness decreasing. Fig. 7d shows the variation of hardness in the X-Y cross-section with respect to different laser powers along the perpendicular direction of the scan track. The hardness decreases from the center to the edge for all laser powers, and the highest hardness was found in the MG processed with laser power of 120 W: ~ 4.6 GPa at the center and ~ 4.0 GPa at the edge, which are similar to the hardness of as-atomized $Al_{86}Ni_6Y_{4.5}Co_2La_{1.5}$ MG powder (~ 4.3 GPa) but lower than the heat treated $Al_{86}Ni_6Y_{4.5}Co_2La_{1.5}$ MG powder with face centered cubic (fcc) Al crystals (~ 8.0 GPa) [23]. The lowest hardness value was found in the MG processed with laser power of 80 W: ~ 4.0 GPa for the center and ~ 3.1 GPa for the edge.

In Fig. 8, the variation of elastic modulus of the MG processed with different laser powers in the X-Y and Z cross-sections is shown. It is apparent that the modulus has a very similar trend as the hardness (Fig. 7). The exception is the horizontal profile of the vertical cross-section (Fig. 8a). In this case, the elastic modulus of the MG processed with laser powers of 200, 160 and 120 W is almost identical (~ 100, 85 and 105 GPa for center, middle and edge, respectively). At a power of 80 W, the modulus is lower (70 GPa) and essentially independent of position.

To assess the plastic deformation behavior of the MG processed by different laser powers, the strain rate dependent serrated flow behavior was obtained using nanoindentation at the center of each laser scan track in the X-Y cross-section (i.e. point I in Fig. 7e). The results are shown in Fig. 9. It is apparent that the depth of indentation varies with the laser power. The maximum indentation depth was found in MG processed with laser power of 120 W, followed by laser power of 200 W and 160 W, while the lowest depth at a laser power of 80 W. This is consistent with the hardness value shown in Fig. 7d. A transition from serrated flow to a non-serrated flow behavior was observed in all four tracks and is arrowed in Fig 9. The lower the strain rate the more obvious the serrated

flow is strain rate sensitive, which has also been shown in other MG materials [24]. However, this transition happens at different strain rates and different depth among the $Al_{86}Ni_6Y_{4.5}Co_2La_{1.5}$ MG scan tracks formed with different laser powers. Decreasing the laser power from 200 W to 120 W increases the strain rate at which the transition occurs (from ~ 1.0 to 2.3 s^{-1}) and also decreases the depth from ~ 25 to 10 nm (Figs. 9a to c). At 80 W, the transition strain rate increases and depth decreases to ~ 0.2 s^{-1} and ~ 60 nm, respectively (Fig. 9d).

4. Discussion

4.1 Melt Pool Morphology

The structure of SLM fabricated components depends on the morphology and the solidification microstructure of the melt pool after each laser scan. The morphology of the melt pool is influenced by the spatial energy distribution of the laser and the heat transfer process within the melt pool [25]. Heat transfer within the melt pool is mainly through convection and conduction, while radiation is negligible [25]. Therefore, the morphology of the melt pool can be determined by the relative proportion of convection and conduction, which can be estimated from the Peclet number (PE) as defined below [25, 26]:

$$PE = \frac{Heat\ transfer_{convection}}{Heat\ transfer_{conduction}} = \frac{\mu \rho C_p r}{k} \tag{2}$$

Where μ is typical liquid velocity, ρ is the density, C_p is the specific heat, r is the radius of the melt pool, and k is the thermal conductivity. If the value of PE is much large than 1, the convection plays a dominant role in heat transfer within the melt pool. Since the coefficient of the surface tension is negative in metals [25] and the Gaussian distribution of

the laser energy (TEM_{00}, $M^2 < 1.05$) results in the center of the melt pool having a higher temperature [27], the liquid flows from the center of the melt pool to the edge.

As the laser power increases, there is clearly an increase in the size of the melt pool (Fig. 3) and therefore, according to Eq. (2), convection becomes more dominant in heat transfer mechanism. As mentioned above, since the specific heat and the thermal conductivity of each laser track is almost the same, the conduction along different directions can be considered identical. However, the convective heat flow mainly occurs along the direction from the center to the edge in the X-Y cross-section (Fig. 2). Hence, this liquid flow (convection) will make the heat dissipate much faster perpendicular to the scanning direction (in the X-Y cross-section in Fig. 2) than other directions (i.e. in the Z direction; Fig. 3). The temperature gradient is therefore larger along the horizontal direction than along the vertical direction. At an angle of 45º the temperature gradient lies between these two extremes. This, together with the Gaussian distribution of the laser beam, causes a Gaussian distribution-like morphology of the melt pool where the width is smaller than the depth. When decreasing the laser power, the width of the melt pool decreases and the PE number decreases accordingly. This implies that the convection heat transfer weakens compared to the conduction. The result of this is that the temperature gradient along the horizontal direction decreases, which causes an increase in the melt width to depth ratio and a gradual change towards the sub-circular morphology of laser scan track shown in Fig. 3d.

4.2 Cracking

The thermal stress developed during the SLM process due to the high and rapid temperature changes can be expressed as [28]:

$$\sigma = \frac{E\alpha}{1-\upsilon}(T_i - T_f) \tag{3}$$

Where E is elastic modulus, α is the coefficient of thermal expansion and υ is Poisson's ratio, which are all material-related properties and hence can be regarded constant in this work. The T_i and T_f are the initial and final temperature of the laser scan track, the former of which will be dependent on the laser power. Due to the Gaussian distribution of the laser beam energy, there is likely to be a spatial variation in the maximum temperature reached within a scan track. Consequently, the temperature drop ($T_i - T_f$) will also vary along the vertical direction within the melt pool. This is the origin of the thermal stresses vertical to the scanning direction. On the other hand, as the laser is scanning across the powder bed, the rapid melting and solidification of materials would cause an expansion and contraction along the scanning direction as well. With increasing the laser power, the relative temperature drop between the center and edge part will also increase which, according to Eq. 3, will induce higher residual stresses. This will tend to result in a higher degree of cracking, as shown in Figs. 2a and b. The cracks formed at 45º to the scanning direction (Fig. 2a) are a result of the combined thermal stresses along vertical and parallel directions. When decreasing the laser power, the induced thermal stress is lowered and at some point the strength of the scan track can accommodate this thermal stress, resulting in a crack-free scan track, as shown in Fig. 2c. At the lowest laser power (80 W), although the thermal stress is reduced, the strength of the laser track is poor due to the presence of large pores. As such, the material cannot withstand the generated thermal stress and cracks again form, as shown in Fig. 2d.

4.3 Devitrification

According to previous studies on laser processing of crystalline and non-crystalline materials, higher laser energies result in a higher local cooling rate due to a greater temperature difference between the melt pool and surrounding material [27, 29]. This higher cooling rate should favor the retention of the amorphous nature of the $Al_{86}Ni_6Y_{4.5}Co_2La_{1.5}$ MG. However,

the results shown in Fig. 4 show the opposite effect; that is higher laser power leads to increased crystallization of the MG. The fabrication process of MG materials through rapid cooling generally requires a chemical homogenous glass-forming alloy melt of high purity [30]. During laser melting, the high laser power may be altering the chemical homogeneity of the liquid, possibly due to the formation of liquid oscillation or capillary wave within the laser scan track [31]. Such a formation could be the result of a pressure wave triggered by the high laser power [31]. All these factors could combine to cause chemical inhomogeneity within the melt pool, which would be much more severe at higher laser power. The chemical distribution within the melt pool is difficult to measure during the SLM process due to the small melt volume and very short interaction time. SEM energy dispersive spectroscopy (EDS) was used to measure the distribution of the major element (Al) and the results are shown in Fig. 10.

Another possibility for the crystallization is increased oxidation. The higher peak temperature at the high laser power increases the possibility of oxidation during SLM [32]. Oxidation is detrimental to the chemical homogeneity of a MG material and tends to increase the ease at which crystallization occurs [33]. Thus, increased oxidation may be another reason for the severe crystallization at the highest laser power. Irrespective of the mechanism, it is apparent that high laser powers should be avoided in order to prevent devitrification of the MG.

At higher laser powers, the material in the HAZ is expected to get hotter for longer, which leads to a greater degree of crystallization in the material immediately adjacent to the melt pool, as shown in Fig. 5. It is apparent that the width of the HAZ increases with increasing laser power and the crystallization becomes more severe, which is consistent with previous studies [34]. As the amount of heat dissipated through the HAZ decreases (i.e. at lower laser powers), there is a gradual decrease in both the size and degree of orientation of the crystals. This suggests that the preferred orientation is a combined result of the heat transfer process

and the devitrification process during the solidification of $Al_{86}Ni_6Y_{4.5}Co_2La_{1.5}$ MG. The competition between these two factors plays a critical role in determination of the final phase formation. Further away from the melt pool (Fig. 6), the amount of crystallised material gradually decreases and there is a distinct interface beyond which the amorphous structure has been retained. In this area, it is apparent that the material has not received sufficient heating to trigger crystallization. However, it is possible that the material has still undergone a certain degree of relaxation due to the dissipated heat from the melt pool.

4.4 Mechanical Properties

The hardness, elastic modulus and the plastic deformation behavior of the $Al_{86}Ni_6Y_{4.5}Co_2La_{1.5}$ MG at different regions of the scan track depend on the local microstructure of the material, e.g. phase formation, free volume, nano pores and etc. [35, 36]. As mentioned above, the fiber laser energy density can be considered a Gaussian distribution. This will cause different parts of the melt pool to have a differing thermal history, such as varying heating and cooling rates as well as different peak temperatures. As such, the densification, phase formation, residual stress and free volume content, will vary at different regions of the solidified MG. This may be able to be used to explain the variation in hardness of the $Al_{86}Ni_6Y_{4.5}Co_2La_{1.5}$ MG in Fig. 7. For example, along the horizontal direction in the Z cross-section in Fig. 7a, the cooling rate will decrease from the center to the edge due to the edge's lower in peak temperature (as a result of the laser's Gaussian distribution). This decreased cooling rate will cause reduction in the free volume content, which may explain the higher hardness at the edge (position 3) compared to the center (position 1) and middle (position 2) when the laser powers are 120, 160 and 200 W. Similar results have been reported in Zr-based MG [37]. On the other hand, the lower cooling rate at the edge of the scan track and the low GFA of the $Al_{86}Ni_6Y_{4.5}Co_2La_{1.5}$ MG [19], may result in the amorphous matrix undergoing slight local ordering processes, promoting the formation of crystalline

nano clusters. This ordering may cause the hardness to increase from the center (position 1) to the edge (position 3) in Fig. 7a. The local ordering trend is also consistent with the observed elongated crystals, where massive local ordering process has taken place, at the edge of the scan track (Fig. 5). In addition, hardness of a MG can also be affected by the residual stress within the material. For example, it has been reported that the hardness of a MG will decrease significantly under an applied tensile stress while only slightly increase under a compressive stress [38]. According to previous studies [6, 7] and above discussion on residual and thermal stresses, a maximum tensile stress is expected to be around position 2 (or II) (Fig. 7e), which coincides with the location of the crack parallel to the scanning direction shown in Fig. 2. The residual tensile stress may account for the decrease of hardness from the center (position 1) to the middle (position 2) in Fig. 7a, despite the reduction of free volume. Therefore, the hardness variation is a combined competition result of free volume and residual stress, both of which are affected by the different thermal history within the scan track.

Although in general hardness and elastic modulus of MG materials vary together, occasionally they have been reported to change in opposite directions on partial crystallized $Al_{86}Ni_6Y_{4.5}Co_2La_{1.5}$ MG powder [39]. This was attributed to the different physical origin of the hardness and elastic modulus. Apart from the abovementioned factors which are related to hardness, the elastic modulus can be influenced by the morphology and distribution of the formed phases. It reflects the strength of the chemical bonding between different elements within the material [40]. These differences may be the reason for the slight variation between the hardness and elastic modulus observed at the center part of the laser scan track in the X-Y cross-section in this study (Figs. 7a and 8a).

It has been reported that the serrated flow during mechanical testing of a MG material is related to the formation and propagation of shear bands, which play a critical role in

determination of the room temperature plasticity [41, 42]. Although the MG laser scan tracks are produced using the same $Al_{86}Ni_6Y_{4.5}Co_2La_{1.5}$ MG powder, the different microstructure and phase formation among those laser scan tracks arising from different thermal history (as shown in Figs. 2 and 4) will cause different formation and propagation of shear bands in each scan track. This difference may explain the different transition from the serrated flow to a non-serrated flow behavior among those MG laser scan tracks as observed in Fig. 9.

5. Conclusion

In this study, the densification, microstructure and mechanical properties of $Al_{86}Ni_6Y_{4.5}Co_2La_{1.5}$ MG processed by SLM single line scans were investigated with respect to different laser powers and the following points are drawn from this study:

(1) The morphology of the laser scan track is influenced by the energy density distribution of the laser spot and the heat transfer process within the melt pool. The energy density distribution plays a more dominant role compared to the heat transfer process at high laser power and the vertical cross-section of the scan track has a Gaussian-distribution like morphology. At low laser power, it is the heat transfer process that dictates the morphology of the laser track, which tends to increase the width while decrease the depth of the scan track.

(2) High laser power will induce high thermal stress which causes the formation of cracks within the solidified laser scan track. At a very low laser power, there is insufficient energy to melt all the powder particles, resulting in the formation of large scaled porosity. This will reduce the strength of the solidified MG, again resulting in the formation of the cracks. In order to produce crack-free material the use of the correct laser power is critical. This is a balance between the thermal stress and the strength of the MG.

(3) Due to the energy density distribution of the fiber laser and the heat transfer process during the SLM process, different regions of the solidified scan track together with the HAZ have a different thermal history, especially the cooling rate, which affects the microstructure and hence hardness, elastic modulus and plasticity behavior. These, including the width, microstructure and phase transformation of the scan track and HAZ, and the mechanical properties of the scan track, can be tailored by using different laser powers. This would provide another feasible way to produce a heterogeneous microstructure of MG, with possible benefits to the plasticity of the fabricated MG. Although high laser power should result in a high cooling rate during SLM (which is in favor of retaining the amorphous nature of MG), the thermal fluctuation within the melt pool will be enhanced at high laser power, causing inhomogeneous chemical distribution and further severe crystallization as a consequence.

Acknowledgments

This work was supported by the Australian Research Council (ARC) Discovery Project DP130103592. The authors gratefully acknowledge Prof. Jianqiang Wang from Institute of Metal Research (IMR), China for the supply of metallic glass powder and Dr. Hisashi Imai from Osaka University, Japan for the spark plasma sintering experiments. The authors also acknowledge the facilities, and the scientific and technical assistance of the Australian Microscopy & Microanalysis Research Facility at the Centre for Microscopy, Characterisation & Analysis, The University of Western Australia, a facility funded by the University, State and Commonwealth Governments.

References

[1] D.D. Gu, W. Meiners, K. Wissenbach, R. Poprawe, Int. Mater. Rev., 57 (2012) 133-164.

[2] L. Thijs, K. Kempen, J.-P. Kruth, J. Van Humbeeck, Acta Mater., 61 (2013) 1809-1819.

[3] L.C. Zhang, D. Klemm, J. Eckert, Y.L. Hao, T.B. Sercombe, Scripta Mater., 65 (2011) 21-24.

[4] K.N. Amato, S.M. Gaytan, L.E. Murr, E. Martinez, P.W. Shindo, J. Hernandez, S. Collins, F. Medina, Acta Mater., 60 (2012) 2229-2239.

[5] H. Attar, M. Calin, L.C. Zhang, S. Scudino, J. Eckert, Materials Science and Engineering: A, 593 (2014) 170-177.

[6] K. Dai, L. Shaw, Acta Mater., 49 (2001) 4171-4181.

[7] P. Mercelis, J.-P. Kruth, Rapid prototyp. J., 12 (2006) 254-265.

[8] A. Inoue, K. Ohtera, A.P. Tsai, T. Masumoto, Jpn.J.Appl.Phys.Part2,Lett., 27 (1988) L479-L482.

[9] B.J. Yang, J.H. Yao, J. Zhang, H.W. Yang, J.Q. Wang, E. Ma, Scripta Mater., 61 (2009) 423-426.

[10] X. Wei, F. Han, X. Wang, X. Wang, C.e. Wen, J. Alloys Compd., 501 (2010) 164-167.

[11] X.P. Li, M. Yan, H. Imai, K. Kondoh, J.Q. Wang, G.B. Schaffer, M. Qian, Mater. Sci. Eng., A, 568 (2013) 155-159.

[12] X.P. Li, M. Yan, G.B. Schaffer, M. Qian, Intermetallics, 39 (2013) 69-73.

[13] X.P. Li, M. Yan, G. Ji, M. Qian, J. Nanomater., (2013).

[14] D.C. Hofmann, J.-Y. Suh, A. Wiest, G. Duan, M.-L. Lind, M.D. Demetriou, W.L. Johnson, Nature, 451 (2008) 1085-U1083.

[15] J. Das, M.B. Tang, K.B. Kim, R. Theissmann, F. Baier, W.H. Wang, J. Eckert, Phys. Rev. Lett., 94 (2005).

[16] S. Pauly, S. Gorantla, G. Wang, U. Kuehn, J. Eckert, Nat. Mater., 9 (2010) 473-477.

[17] G. He, W. Loser, J. Eckert, Acta Mater., 51 (2003) 5223-5234.

[18] S. Pauly, L. Loeber, R. Petters, M. Stoica, S. Scudino, U. Kuehn, J. Eckert, Mater. Today, 16 (2013) 37-41.

[19] X.P. Li, M. Yan, B.J. Yang, J.Q. Wang, G.B. Schaffer, M. Qian, Mater. Sci. Eng., A, 530 (2011) 432-439.

[20] L. Thijs, F. Verhaeghe, T. Craeghs, J. Van Humbeeck, J.-P. Kruth, Acta Mater., 58 (2010) 3303-3312.

[21] A. Simchi, H. Pohl, Mater. Sci. Eng., A, 359 (2003) 119-128.

[22] W.C. Oliver, G.M. Pharr, Journal of Materials Research, 7 (1992) 1564-1583.

[23] X.P. Li, M. Yan, J.Q. Wang, M.Y. Lu, G.B. Schaffer, M. Qian, Intermetallics, 30 (2012) 117-121.

[24] C.A. Schuh, T.G. Nieh, Acta Mater., 51 (2003) 87-99.

[25] G.G. Roy, J.W. Elmer, T. DebRoy, J. Appl. Phys., 100 (2006).

[26] R. Rai, S.M. Kelly, R.P. Martukanitz, T. Debroy, Metall. Mater. Trans. A, 39A (2008) 98-112.

[27] S. Katakam, J.Y. Hwang, S. Paital, R. Banerjee, H. Vora, N.B. Dahotre, Metall. Mater. Trans. A, 43A (2012) 4957-4966.

[28] S. Katakam, S. Santhanakrishnan, H. Vora, J.Y. Hwang, R. Banerjee, N.B. Dahotre, Philos. Mag. Lett., 92 (2012) 617-624.

[29] B. Zheng, Y. Zhou, J.E. Smugeresky, E.J. Lavernia, Metall. Mater. Trans. A, 40A (2009) 1235-1245.

[30] W.H. Wang, C. Dong, C.H. Shek, Mater. Sci. Eng., R, 44 (2004) 45-89.

[31] W.D. Liu, L.M. Ye, K.X. Liu, J. Appl. Phys., 109 (2011).

[32] Y.N. Zhang, X. Cao, P. Wanjara, M. Medraj, Acta Mater., 61 (2013) 6562-6576.

[33] Z.P. Lu, C.T. Liu, W.D. Porter, Appl. Phys. Lett., 83 (2003) 2581-2583.

[34] H. Sun, K.M. Flores, Metall. Mater. Trans. A, 41A (2010) 1752-1757.

[35] J. Eckert, J. Das, S. Pauly, C. Duhamel, J. Mater. Res., 22 (2007) 285-301.

[36] J.F. Loffler, Intermetallics, 11 (2003) 529-540.

[37] W. Zhao, G. Li, Y.Y. Wang, R.P. Liu, J. Non-Cryst. Solids, 358 (2012) 3318-3321.

[38] L. Wang, H. Bei, Y.F. Gao, Z.P. Lu, T.G. Nieh, Acta Mater., 59 (2011) 2858-2864.

[39] X.P. Li, M. Yan, J.Q. Wang, H. Huang, C. Kong, G.B. Schaffer, M. Qian, J. Alloys Compd., 530 (2012) 127-131.

[40] L.Q. Xing, C. Bertrand, J.P. Dallas, M. Cornet, Mater. Sci. Eng., A, 241 (1998) 216-225.

[41] B.A. Sun, S. Pauly, J. Tan, M. Stoica, W.H. Wang, U. Kuehn, J. Eckert, Acta Mater., 60 (2012) 4160-4171.

[42] G. Wang, K.C. Chan, L. Xia, P. Yu, J. Shen, W.H. Wang, Acta Mater., 57 (2009) 6146-6155.

Figure captions

Fig. 1 A schematic illustration of the single line scan performed through SLM on a SPS fabricated $Al_{86}Ni_6Y_{4.5}Co_2La_{1.5}$ MG.

Fig. 2 SEM BSE images of the scan tracks formed with different laser powers during SLM in the X-Y cross-section: (a) 200 W; (b) 160 W; (c) 120 W; and (d) 80 W. Arrows (in red) point to pores and arrows (in white) point to cracks.

Fig. 3 SEM BSE images of the scan tracks formed with different laser powers during SLM in the Z cross-section: (a) 200 W; (b) 160 W; (c) 120 W; and (d) 80 W. Arrows (in red) point to pores.

Fig. 4 SEM BSE images of the centre region of the scan tracks in the SLM processed $Al_{86}Ni_6Y_{4.5}Co_2La_{1.5}$ MG with different laser powers: (a) 200 W; (b) 160 W; (c) 120 W; and (d) 80 W. Arrows (in red) point to low Al content areas and arrows (in white) point to high Al content areas.

Fig. 5 SEM BSE images of the edge region of the scan tracks in the SLM processed $Al_{86}Ni_6Y_{4.5}Co_2La_{1.5}$ MG (X-Y cross-section) with different laser powers: (a) 200 W; (b) 160 W; (c) 120 W; and (d) 80 W. Arrows (in red) point to equiaxed crystals and arrows (in white) point to elongated crystals.

Fig. 6 SEM BSE images of the HAZ in the SLM processed $Al_{86}Ni_6Y_{4.5}Co_2La_{1.5}$ MG. The HAZ of different scan tracks (either in the X-Y or Z cross-sections) with different laser powers show similar microstructure and phases except for the width of the HAZ, therefore only the HAZ of scan track formed with laser power of 120 W are shown here. The approximate distance L from the observed microstructure and phases to the melt pool is also shown in each figure.

Fig. 7 Hardness of the SLM processed $Al_{86}Ni_6Y_{4.5}Co_2La_{1.5}$ MG at different regions of the scan tracks: (a) to (c) Z cross-section; (d) X-Y cross-section. The position of the indents is marked with numbers correspondingly in (e).

Fig. 8 Elastic modulus of the SLM processed $Al_{86}Ni_6Y_{4.5}Co_2La_{1.5}$ MG at different regions of the scan tracks: (a) to (c) Z cross-section; (d) X-Y cross-section. The position of the indents is marked with numbers correspondingly in Fig. 7e.

Fig. 9 The serrated flow behavior of the SLM processed $Al_{86}Ni_6Y_{4.5}Co_2La_{1.5}$ MG with different laser powers obtained using nanoindentation at the centre of the track in X-Y cross-section: (a) 200 W; (b) 160 W; (c) 120 W; and (d) 80 W. Arrows show the transition from serrated flow to non-serrated flow behaviour.

Fig. 10 SEM EDS results for the major element Al obtained through line scan across the scan tracks perpendicular to the scanning direction in the X-Y cross-section with different laser powers: (a) 200 W; (b) 160 W; (c) 120 W; and (d) 80 W.

Figure(s)

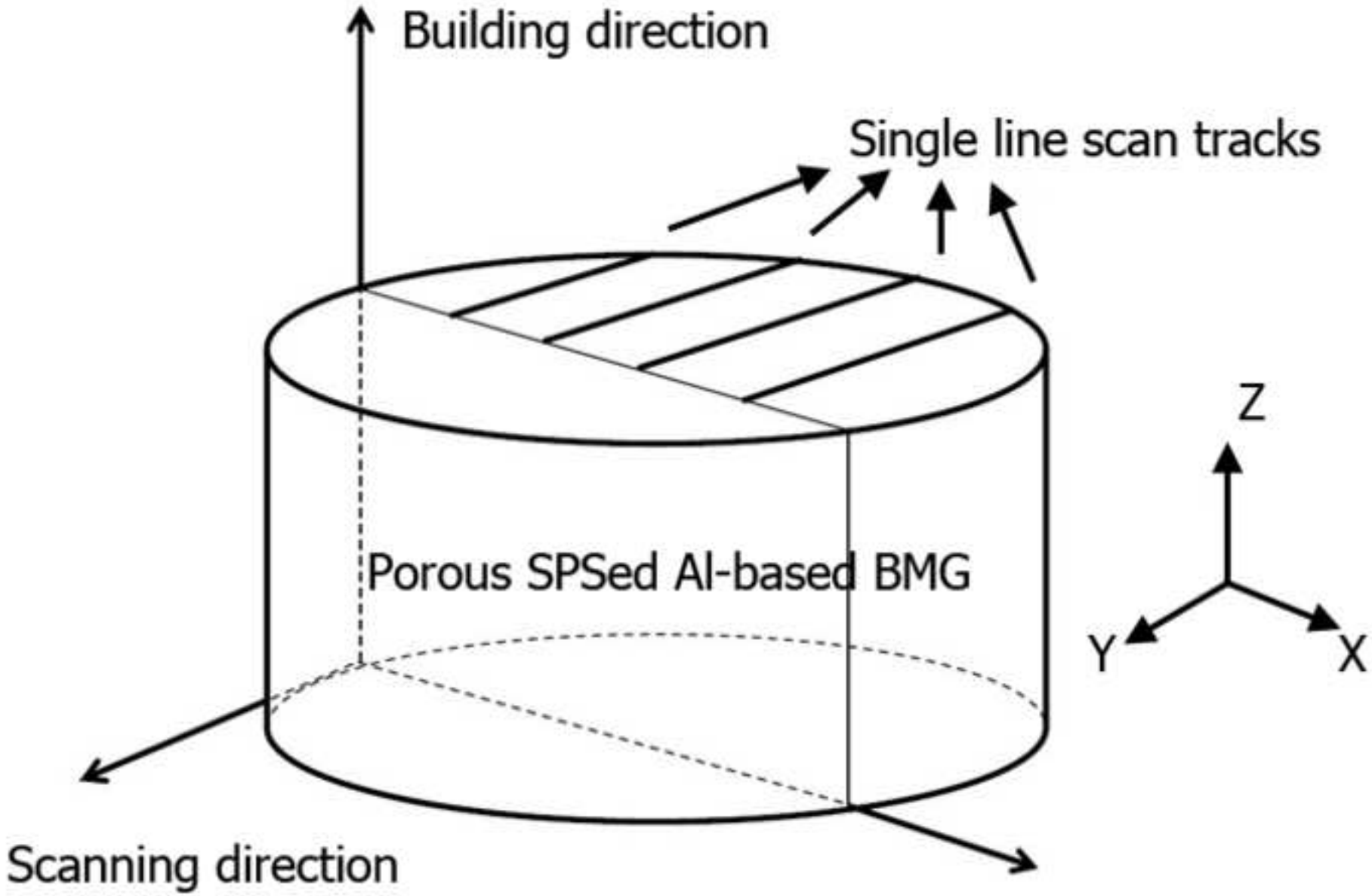

Figure(s)

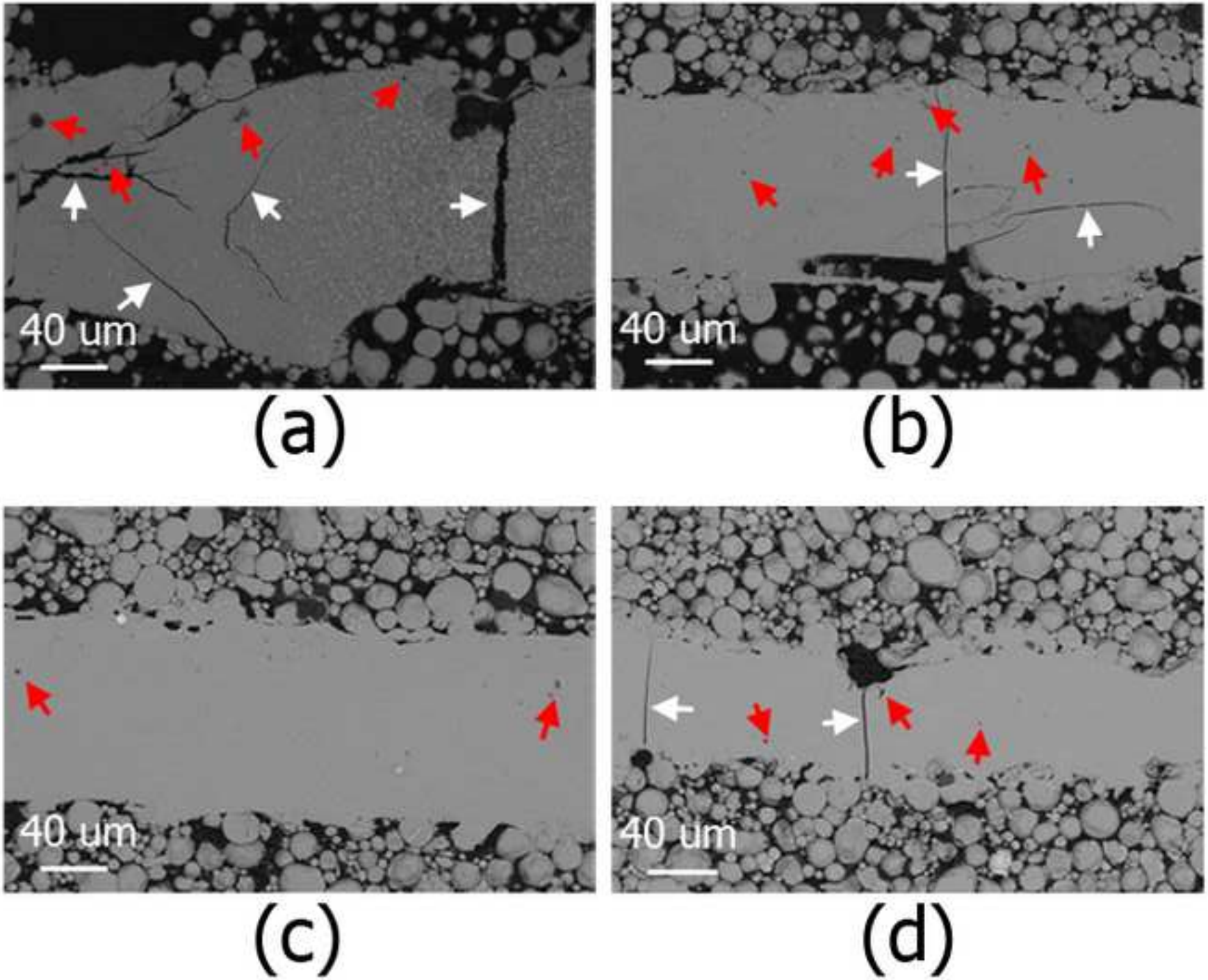

Figure(s)

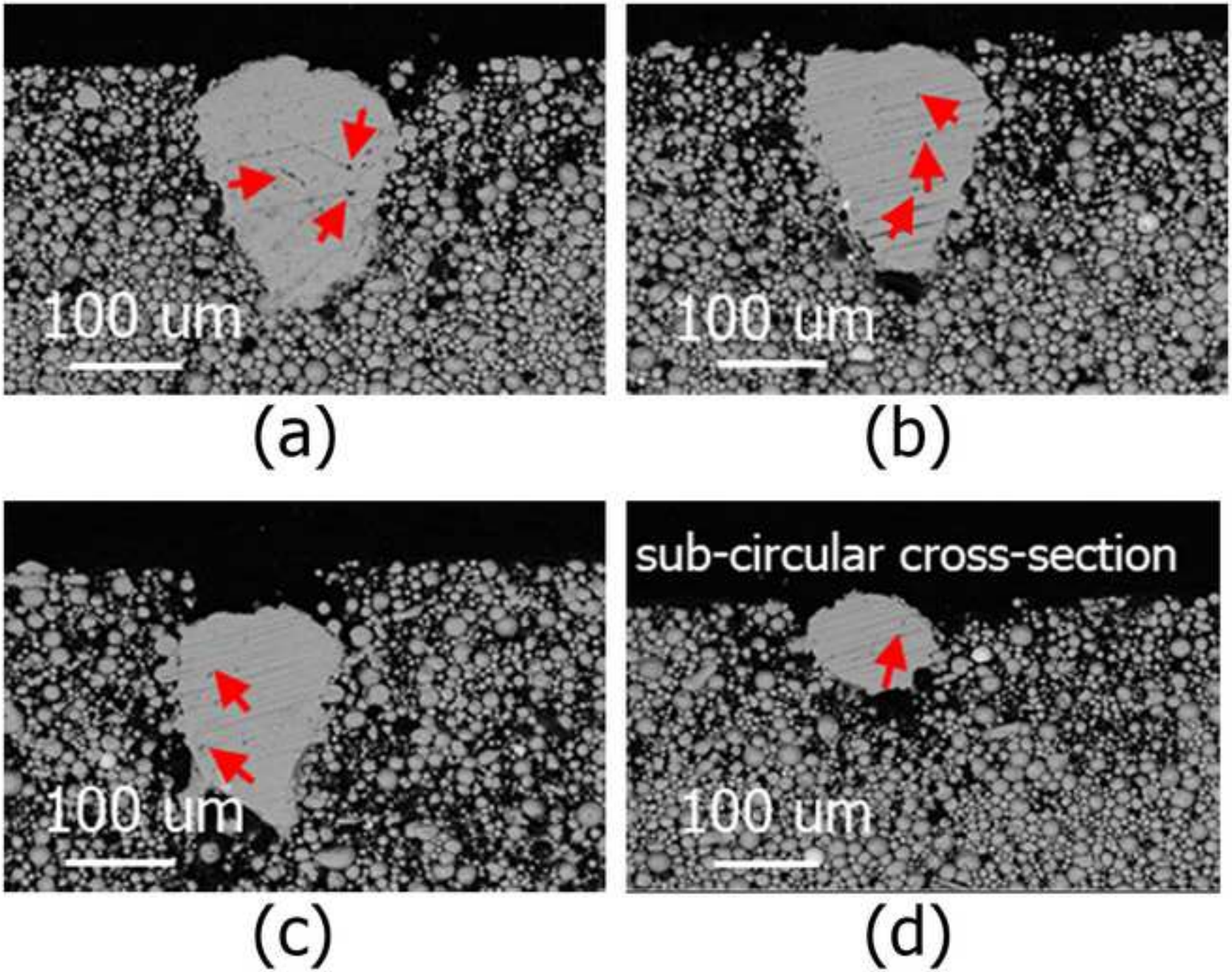

Figure(s)

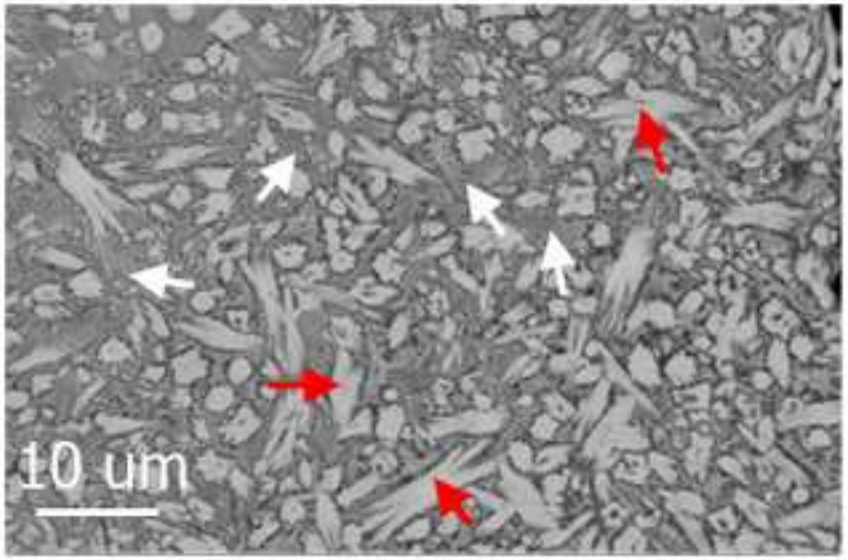

(a)

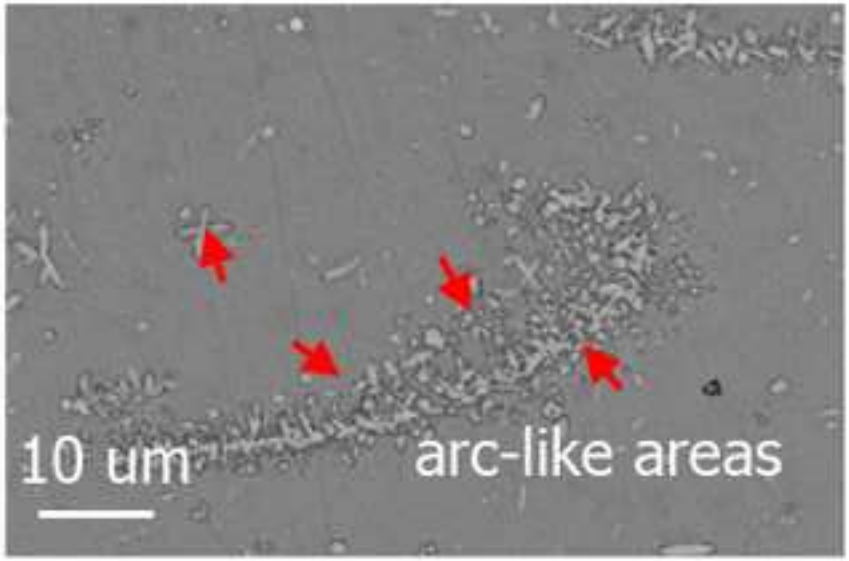

(b)

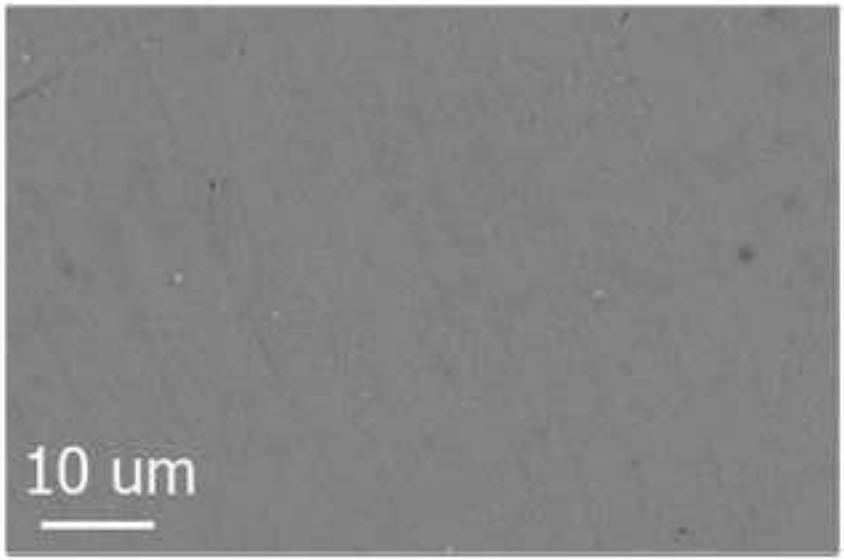

(c)

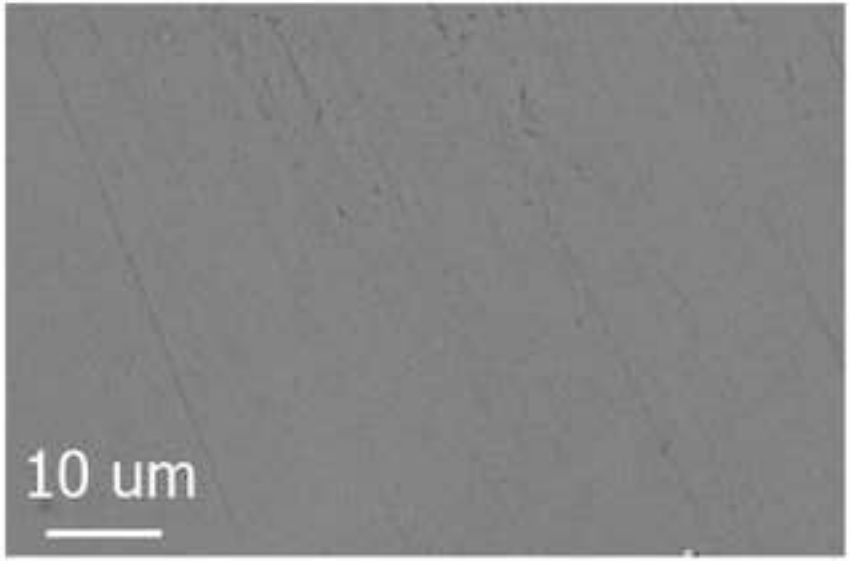

(d)

Figure(s)

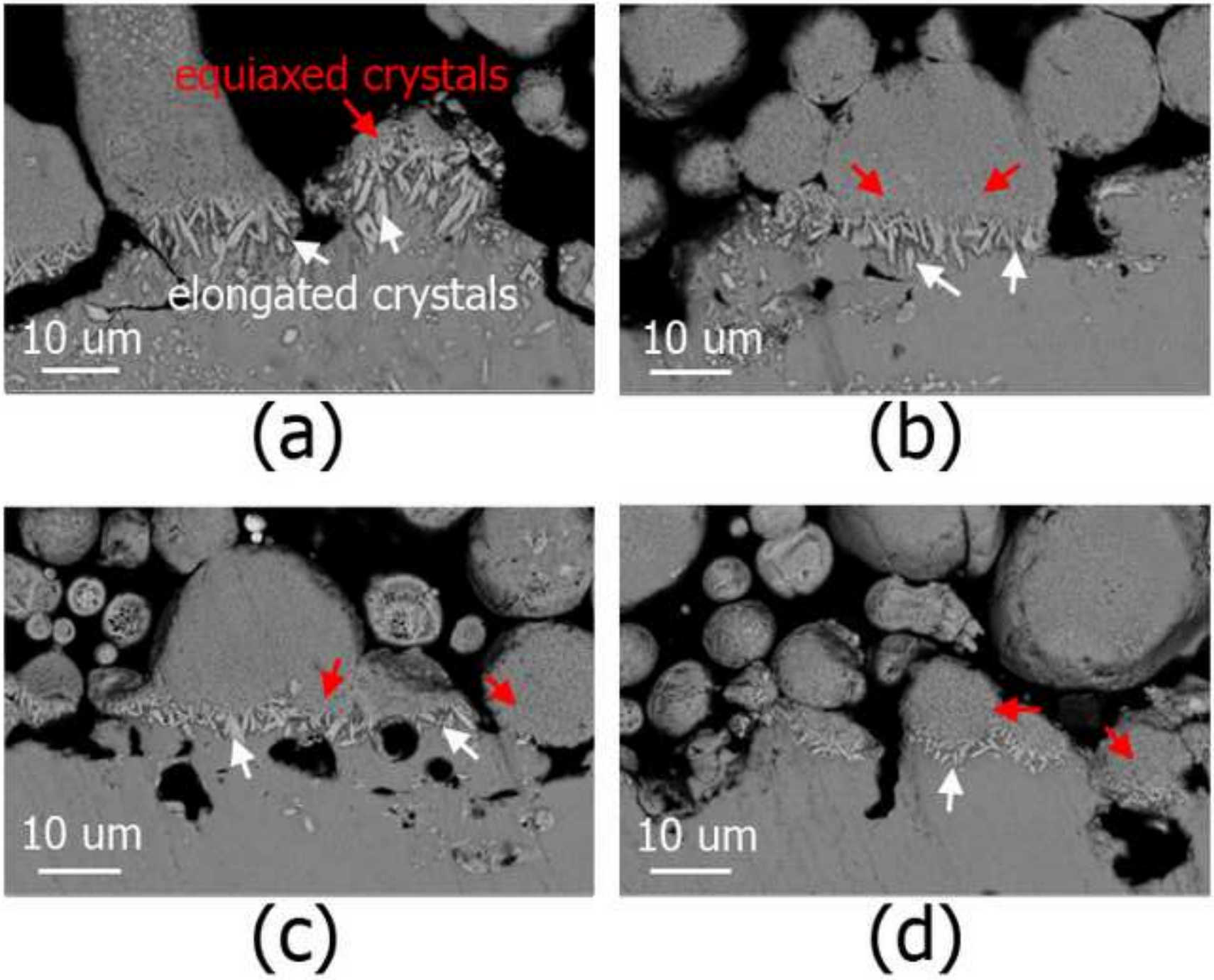

Figure(s)

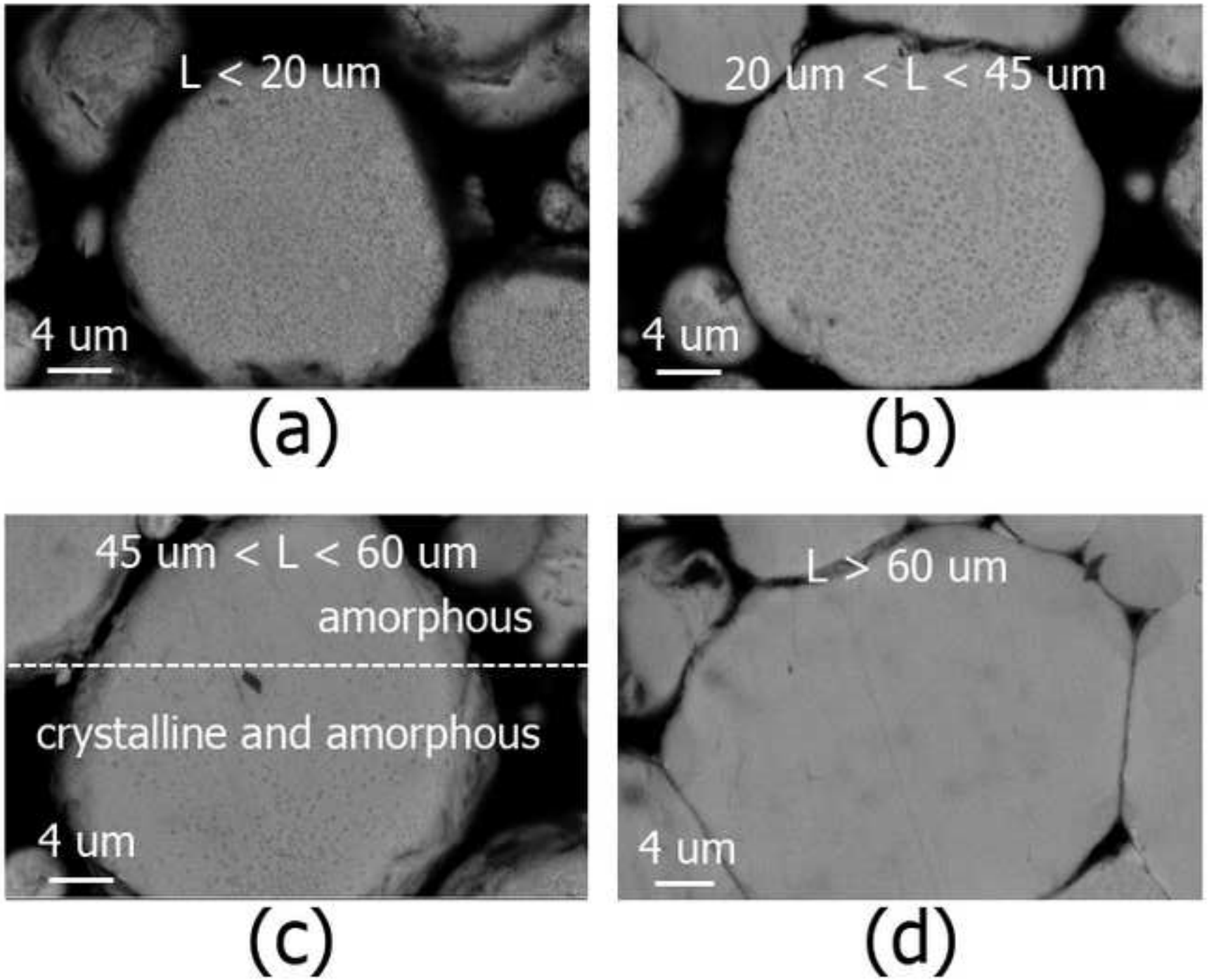

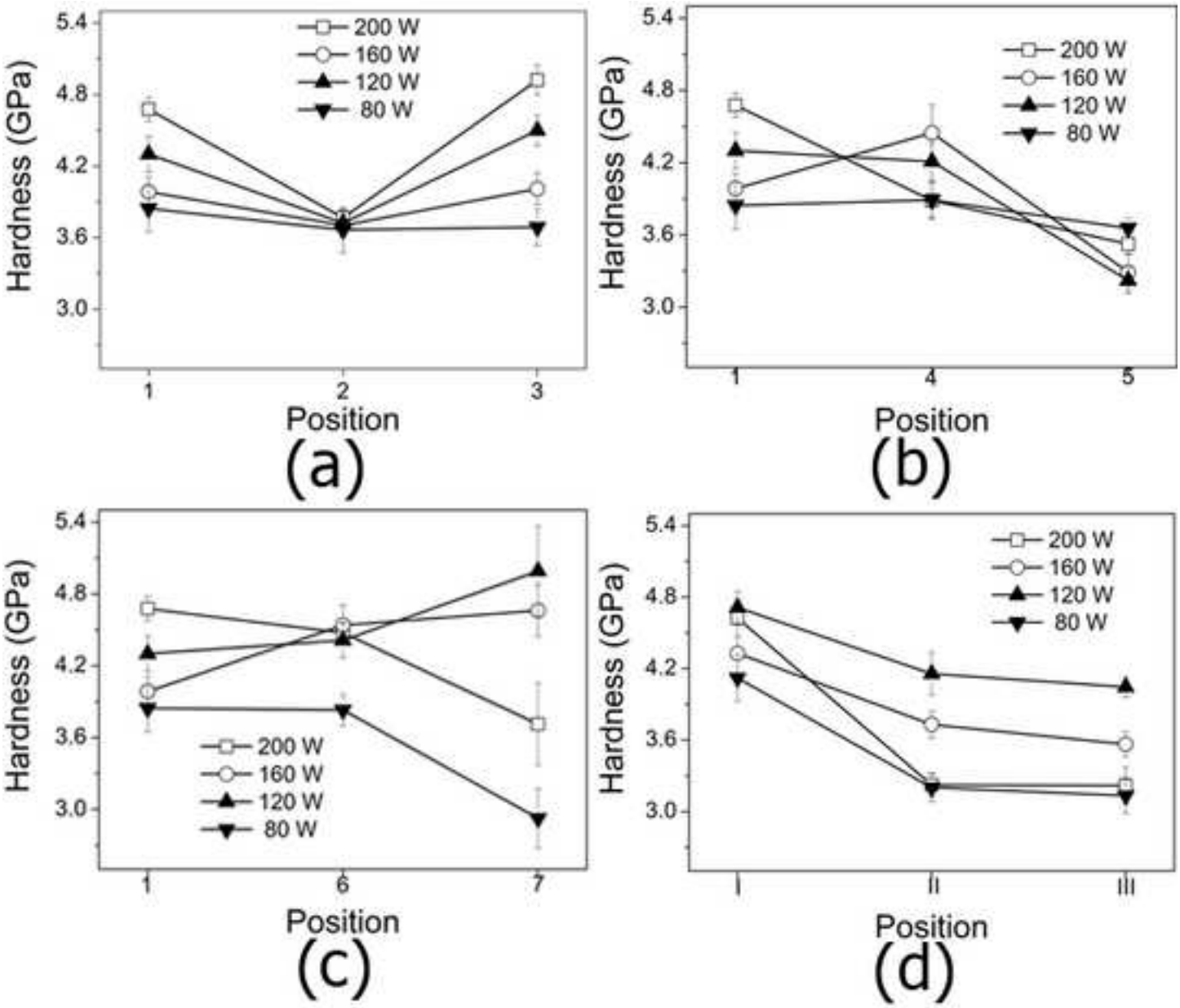

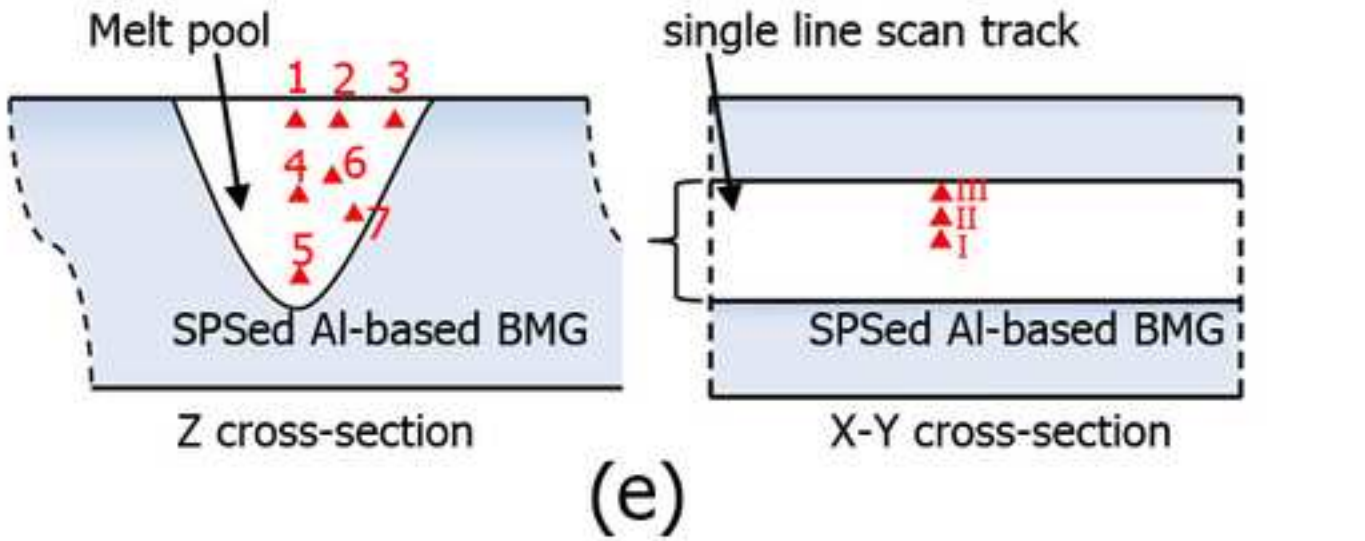

Figure(s)

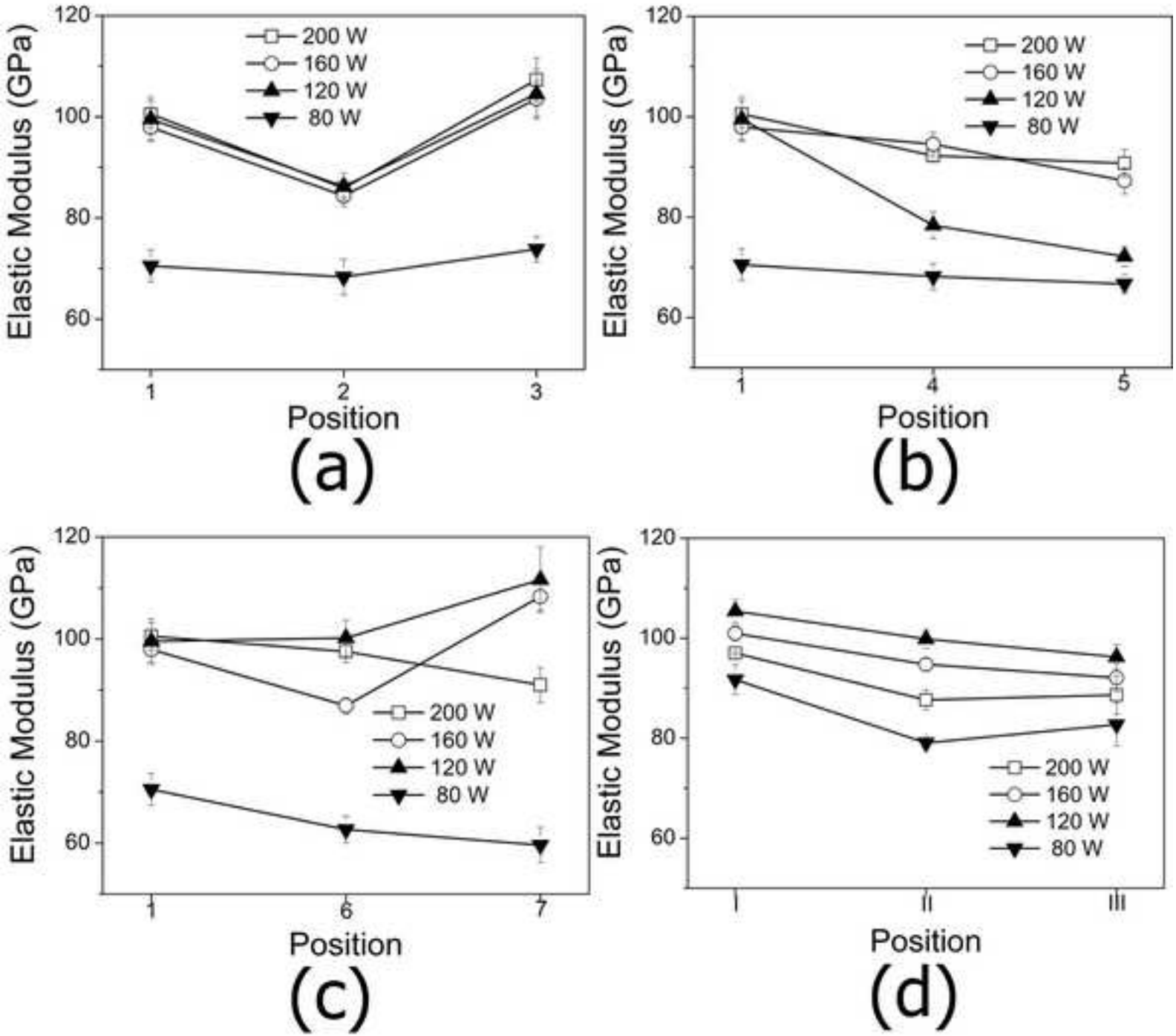

Figure(s)

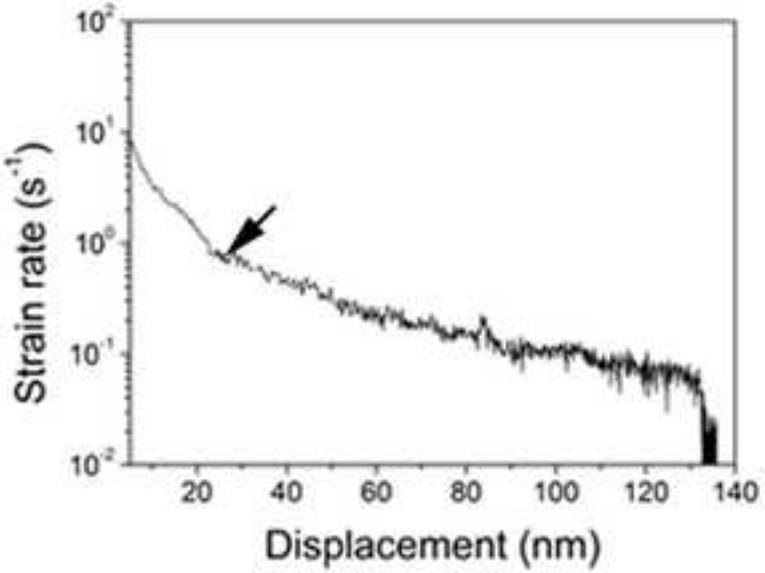

(a)

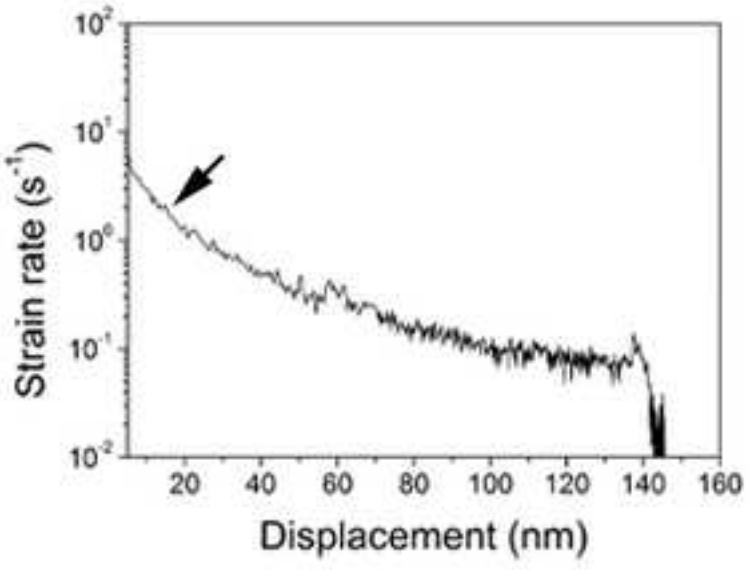

(b)

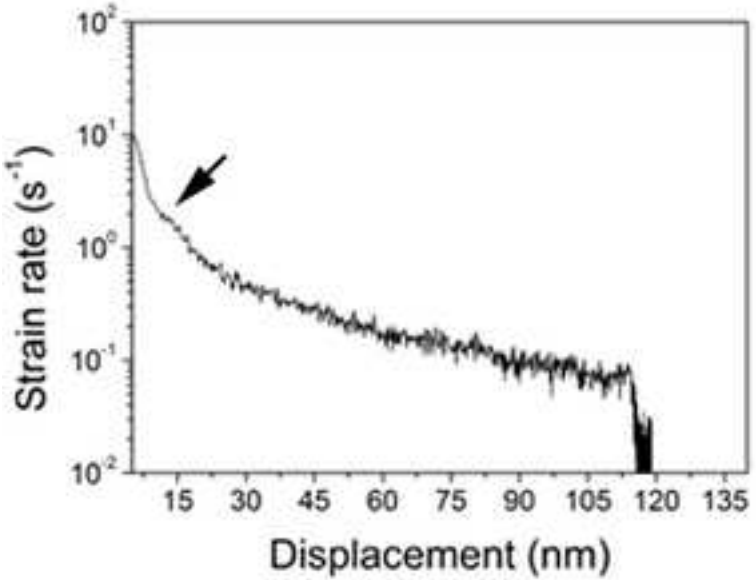

(c)

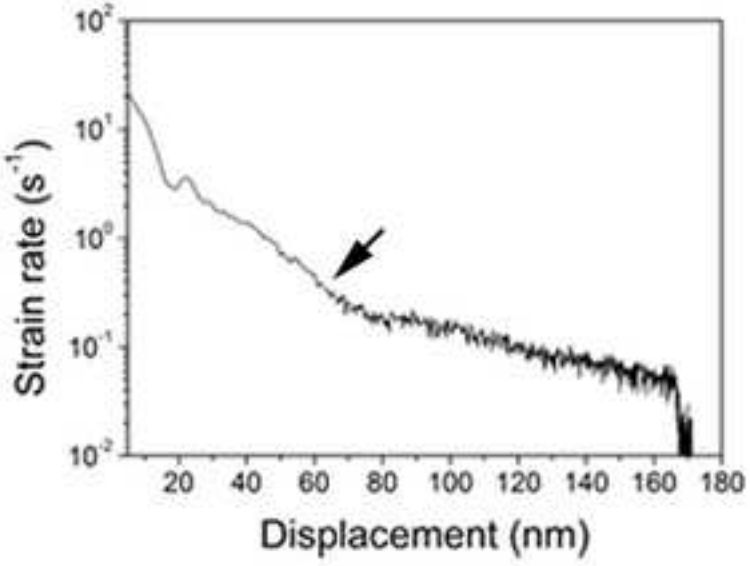

(d)

Figure(s)